

Revealing Donor–Acceptor Interaction on the Printed Active Layer Morphology and the Formation Kinetics for Nonfullerene Organic Solar Cells at Ambient Conditions

Xinyu Jiang, Pauline Chotard, Kexun Luo, Felix Eckmann, Suo Tu, Manuel A. Reus, Shanshan Yin, Julija Reitenbach, Christian L. Weindl, Matthias Schwartzkopf, Stephan V. Roth, and Peter Müller-Buschbaum*

Slot-die coating is a powerful method for upscaling the production of organic solar cells (OSCs) with low energy consumption print processes at ambient conditions. Herein, chlorobenzene (CB) and chloroform (CF) are compared as host solvents for printing films of the neat novel fused-ring unit based wide-bandgap donor polymer (PDTBT2T-FTBDT), the small molecule nonfullerene acceptor based on a fused ring with a benzothiadiazole core (BTP-4F) as well as the respective PDTBT2T-FTBDT:BTP-4F blend films at room temperature in air. Using CF printing of the PDTBT2T-FTBDT:BTP-4F active layer, OSCs with a high power conversion efficiency of up to 13.2% are reached in ambient conditions. In comparison to CB printed blend films, the active layer printed out of CF has a superior morphology, a smoother film surface and a more pronounced face-on orientation of the crystallites, which altogether result in an enhanced exciton dissociation, a superior charge transport, and suppressed nonradiative charge carrier recombination. Based on in situ studies of the slot-die coating process of PDTBT2T-FTBDT, BTP-4F, and PDTBT2T-FTBDT:BTP-4F films, the details of the film formation kinetics are clarified, which cause the superior behavior for CF compared to CB printing due to balancing the aggregation and crystallization of donor and acceptor.


1. Introduction

Organic solar cells (OSCs) have made considerable progress in recent decades due to developing novel materials, improved fabrication pathways, and the implementation of modern measure-

ment technologies.^[1–5] Both novel acceptor molecules and donor polymers contributed to the observed strong increase in power conversion efficiencies (PCEs). In particular, nonfullerene acceptor molecules and wide-bandgap polymer donors provided big improvements. For example, Lin et al. designed the nonfullerene acceptor named 3,9-bis(2-methylene-(3-(1,1-dicyanomethylene)-indanone))-5,5,11,11-tetrakis(4-hexylphenyl)-dithieno[2,3-d:2',3'-d']-s-indaceno[1,2-b:5,6-b']dithiophene (ITIC) to resolve the limitations of a weak absorption in the visible spectral region and limited energy level variability of the fullerenes.^[6] With the development of the wide-bandgap polymer poly[(2,6-(4,8-bis(5-(2-ethylhexyl)thiophen-2-yl)-benzo[1,2-b:4,5-b']dithiophene))-alt-(5,5-(1',3'-di-2-thienyl-5',7'-bis(2-ethylhexyl)benzo[1',2'-c:4',5'-c']dithiophene-4,8-dione)] (PBDB-T) derivatives such as poly[(2,6-(4,8-bis(5-(2-ethylhexyl-3-fluoro)thiophen-2-yl)-benzo[1,2-b:4,5-b']dithiophene))-alt-(5,5-(1',3'-di-2-thienyl-5',7'-bis(2-ethylhexyl)benzo[1',2'-c:4',5'-c']dithiophene-4,8-dione)] (PBDB-T2F or PM6) and poly[(2,6-(4,8-bis(5-(2-ethylhexyl-3-chloro)thiophen-2-yl)-benzo[1,2-b:4,5-b']dithiophene))-alt-(5,5-(1',3'-di-2-thienyl-5',7'-bis(2-ethylhexyl)benzo[1',2'-c:4',5'-c']dithiophene-4,8-dione)]

X. Jiang, P. Chotard, K. Luo, S. Tu, M. A. Reus, S. Yin, J. Reitenbach, C. L. Weindl, P. Müller-Buschbaum
Lehrstuhl für Funktionelle Materialien
Physik Department
Technische Universität München
James-Franck-Str. 1, 85748 Garching, Germany
E-mail: muellerb@ph.tum.de

F. Eckmann
Walter Schottky Institut
Physik Department
Technische Universität München
Am Coulombwall 4, 85748 Garching, Germany
M. Schwartzkopf, S. V. Roth
Deutsches Elektronen-Synchrotron DESY
Notkestraße 85, 22607 Hamburg, Germany
S. V. Roth
Department of Fibre and Polymer Technology
KTH Royal Institute of Technology
Teknikringen 56-58, Stockholm SE-100 44, Sweden
P. Müller-Buschbaum
Heinz Maier-Leibnitz Zentrum (MLZ)
Technische Universität München
Lichtenbergstr. 1, 85748 Garching, Germany

 The ORCID identification number(s) for the author(s) of this article can be found under <https://doi.org/10.1002/aenm.202103977>.

© 2022 The Authors. Advanced Energy Materials published by Wiley-VCH GmbH. This is an open access article under the terms of the Creative Commons Attribution-NonCommercial License, which permits use, distribution and reproduction in any medium, provided the original work is properly cited and is not used for commercial purposes.

DOI: 10.1002/aenm.202103977

(PBDB-T-2Cl or PM7), as well as other donor polymers such as poly[[6,7-difluoro(2-hexyldecyl)oxy]-5,8-quinoxalinediyl]-2,5-thiophenediyl (PTQ10) and poly[(5,6-difluoro-2-octyl-2H-benzotriazole-4,7-diyl)-2,5-thiophenediyl[4,8-bis[5-(2-hexyldecyl)-2-thienyl]benzo[1,2-b:4,5-b']dithiophene-2,6-diyl]-2,5-thiophenediyl] (J51), the efficiency of ITIC-based as well as other novel acceptor based OSCs improved up to 15%.^[7–11] Moreover, Yuan et al. designed a ladder-type ring acceptor named 2,2'-(2Z,2'Z)-((12,13-bis(2-ethylhexyl)-3,9-diundecyl-12,13-dihydro-[1,2,5]thiadiazolo[3,4 e]thieno[2'',3'':4',5']thieno[2',3':4,5]pyrrolo[3,2 g] thieno [2'',3'':4,5] thieno[3,2-b]indole-2,10-diyl)bis(methanylylidene))bis(5,6-difluoro-3-oxo-2,3-dihydro-1H-indene-2,1-diylidene)dimalononitrile (BTP-4F or sometimes called Y6) with an electron-deficient core, which improved the PCE to 15.7% by combining it with the polymer donor PBDBT-2F in bulk heterojunction (BHJ) type active layers.^[12] Recently, Ding et al. designed a new dithieno[3',2':3,4;2'',3'':5,6]benzo[1,2-c][1,2,5]thiadiazole (DTBT) fused-ring unit based donor polymer poly[2,2''-bis[[2-(2-butyldecyl)oxy]carbonyl][2,2':5',2'':5'',2''''-quaterthiophene]-5,5''-diyl] (PDTBT2T-FTBDT or sometimes called D18). It shows a larger molecular plane and higher hole mobility compared with earlier realized polymers. By using this donor polymer in combination with the BTP-4F nonfullerene acceptor as the active layer, the efficiency of single-junction OSCs can reach up to 18%.^[13] However, these high-performance OSCs are commonly fabricated on a small scale in laboratories by using the spin-coating method under inert conditions, which is not suitable for large-scale production.^[14] Therefore, developing a large-area coating technology, which works at ambient conditions, is crucial for manufacturing energy-efficient, high-throughput, low-cost, and low carbon-footprint OSCs.^[15] With the merits of a low solution consumption, high film homogeneity and good device performance, the slot-die coating technique is advantageous in sheet-to-sheet and roll-to-roll (R2R) large-area solution printing. Thus, the slot-die coating is considered as a promising tool for printing large-scale OSCs.^[16–18] However, high efficiency OSCs fabricated by slot-die coating are still not as efficient as those produced by spin-coating due to the absence of a deep understanding of the donor/acceptor formation kinetics during the print process.^[19,20] Today, there are already reports of using slot-die coating for printing OSCs, which could achieve OSCs with an efficiency of over 14% by using additional auxiliary equipment, such as temperature control and atmosphere control assistance.^[21–23] However, such auxiliary equipment has the disadvantage of being more difficult to handle and more expensive concerning commercialization. Based on the above considerations, understanding the relationship between active layer morphology and device efficiency and detailed knowledge about the film formation kinetics is needed for printed BHJ active layers to guide the future photovoltaic performance enhancement. This will be of particularly high relevance for advancing to simplified setups in ambient conditions and without auxiliary equipment to print real-world feasible OSCs. Unfortunately, knowledge gained from the analysis of spin-coating cannot be easily transferred to printing. Besides the different flow fields, the difference between spin-coating and slot-die coating is that the solvent is kept longer in the

polymer film during the film formation procedure for the slot-die coated films without external assistance.^[24–26]

Substantial research proved that the host solvent played a dominant role in the morphology control of the active layer, which influenced the performance of the final devices.^[27–29] By carefully tuning the print parameters, Zhao et al. reported the effects of halogenated and hydrocarbon solvents on PBDBT-2F:BTP-4F active layer based BHJ OSC. A higher degree of crystallinity with a more minor phase separation structure was observed in *ortho*-xylene processed thin films, yielding the promising champion efficiency of 15.6%.^[28] Moreover, some in situ studies were performed to understand the morphology evolution of the active layer processed out of different solvents during the film formation process.^[30,24] However, only a few studies focused on the individual morphology, optical behavior, and film formation kinetics of the donor and acceptor in printed active layers. Understanding the behavior of the pure donor and acceptor components is essential to comprehend how the donor and acceptor affect film formation process of the active layer.

In addition, the understanding of the relatively novel wide-bandgap polymer PDTBT2T-FTBDT is still minimal, since there are only a few reports on this novel material today.^[31,32] Therefore, deep insights into the mechanism of the film formation kinetics of the homopolymer PDTBT2T-FTBDT and of PDTBT2T-FTBDT blended with small acceptor molecules are of great importance to successfully transit from highly efficient spin-coated lab-scale devices to a large scale slot-die coating manufacturing.

In this work, we fabricate slot-die coated BHJ OSCs with an active layer formed by the wide-bandgap donor polymer (PDTBT2T-FTBDT) and a nonfullerene acceptor (BTP-4F) in ambient conditions. The chemical structures of both materials are shown in **Figure 1**. The host solvents chloroform (CF) and chlorobenzene (CB) are selected to tune the morphology of the neat PDTBT2T-FTBDT and BTP-4F films and the PDTBT2T-FTBDT:BTP-4F blend films. Here, we present a room temperature slot-die coated OSC prepared in air with CF as solvent displaying a PCE of 13.2%, which is the highest efficiency reported for printed OSCs in ambient conditions until now. Moreover, no additional postproduction steps like annealing are needed, which reduces the energy consumption in the device fabrication. To further understand the underlying mechanisms and the influence of the used solvent, we study the effect of the specific solvent on the donor and the acceptor performance. The complex relationships between the conformation, charge carrier physics, solvent effects, and the morphology of the printed thin films of PDTBT2T-FTBDT, BTP-4F, and PDTBT2T-FTBDT:BTP-4F blends are investigated with ultraviolet-visible spectroscopy (UV-vis), photoluminescence (PL), time-resolved photoluminescence (TRPL), grazing-incidence small-angle X-ray scattering (GISAXS), atomic force microscopy (AFM), and grazing-incidence wide-angle X-ray scattering (GIWAXS). The results of these measurements can be used to further optimize the photovoltaic device performance for large-scale production of OSCs. Additional in situ UV-vis measurements are performed to further understand the conformational changes with different solvents at ambient conditions during the print process. Moreover, in situ GIWAXS measurements reveal

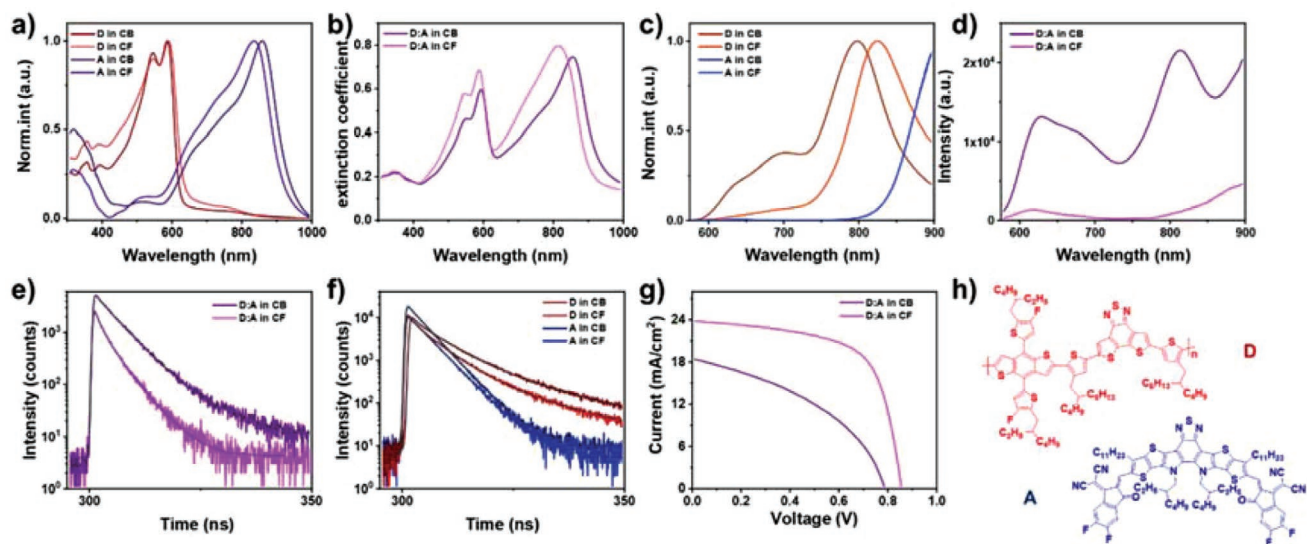


Figure 1. a) Normalized absorption spectra of PDTBT2T-FTBDT and BTP-4F thin films processed with different solvents. b) Extinction coefficients (ϵ_{ex}) of PDTBT2T-FTBDT:BTP-4F blend films printed with different solvents calculated from UV-vis spectra. c) Normalized PL spectra of PDTBT2T-FTBDT and BTP-4F thin films processed with different solvents. d) PL data of PDTBT2T-FTBDT:BTP-4F blend films printed with different solvents. TRPL data of e) PDTBT2T-FTBDT and BTP-4F thin films and f) PDTBT2T-FTBDT:BTP-4F blend films printed with different solvents. g) J - V curves of the best-performing devices based on the printed PDTBT2T-FTBDT:BTP-4F active layers. h) Chemical structures of PDTBT2T-FTBDT (named D in red) and BTP-4F (named A in blue).

information about the influence of the solvents on the donor and acceptor crystal structure and their crystal orientation formation in the active layer. Thereby, our work gives insights into the relationship between the donor-acceptor morphology evolution and optical device properties being influenced by the solvent. Its understanding sets a perspective for large-scale fabrication of OSC via printing under ambient conditions.

2. Results and Discussion

2.1. Optical Properties and Device Performance

The effect of different host solvents on the optical properties is investigated by UV-vis spectroscopy and PL measurements. The corresponding optical parameters are shown in Table S1 (Supporting Information). Normalized UV-vis absorption spectra of printed neat PDTBT2T-FTBDT and BTP-4F thin films fabricated out of CB and CF at ambient conditions are shown in Figure 1a. Most D-A-based polymers such as PDTBT2T-FTBDT or PDBD-T-2F form J-type aggregates and therefore exhibit an intense 0-0 vibronic (λ_{0-0}) absorption band at a higher wavelength with a less intense vibronic progression (λ_{0-1}) at a lower wavelength.^[33] In Figure 1a, the maximum absorption peak (λ_{0-0}) of PDTBT2T-FTBDT is located at 586 nm with a shoulder-type absorption peak (λ_{0-1}) at 545 nm, if processed with CB solvent, while the λ_{0-0} peak red shifts to 590 nm and the λ_{0-1} peak red shifts to 546 nm, if processed with CF solvent. The slight red shifts for the PDTBT2T-FTBDT films printed from CF solvent could be a head-to-tail aggregation preference in comparison with the CB solvent.^[34] Unlike the neat PDTBT2T-FTBDT thin film, the CB processed BTP-4F blend film exhibits an absorption peak at 859 nm, which blue shifts to 835 nm in

case of printing out of CF solvent. This behavior results from a pronounced H-aggregate tendency with a side-by-side arrangement in the CF processed neat BTP-4F film.^[35] The extinction coefficients of the blend films are shown in Figure 1b. The calculation details are explained in the Supporting Information. The CF processed PDTBT2T-FTBDT:BTP-4F blend film exhibits a higher extinction coefficient in the complete spectral range, where PDTBT2T-FTBDT shows a λ_{0-0} peak at 587 nm, a λ_{0-1} peak at 546 nm and BTP-4F one at 809 nm. In contrast, CB processed PDTBT2T-FTBDT:BTP-4F blend films show a lower extinction coefficient. The PDTBT2T-FTBDT λ_{0-0} peak red shifts to 591 nm with a shoulder at 549 nm and the BTP-4F peak redshifts to 858 nm, suggesting preferable J-aggregates in mixtures processed with CB. This aggregation behavior is different from the neat PDTBT2T-FTBDT film. The differences demonstrate that the aggregation type in the printed blend film can be tuned by introducing the nonfullerene acceptor BTP-4F.

In the PL data seen in Figure 1c, the main emission peak of PDTBT2T-FTBDT is located at 798 nm, if printed out of CB. It is significantly red shifted to 825 nm when printed out of CF. The λ_{1-0} emission peak of PDTBT2T-FTBDT is located at 700 nm, if processed with CB and it is significantly suppressed when printed out of CF solvent. No noticeable peak shifts in the BTP-4F films could be determined from the PL spectra. In the blend films (Figure 1d), the CB processed film shows two prominent PL emission peaks located at 629 and 813 nm attributed to PDTBT2T-FTBDT, which suggest that the exciton transport is inhibited from PDTBT2T-FTBDT to BTP-4F. In contrast, the overall PL emission intensity decreases in the CF printed PDTBT2T-FTBDT:BTP-4F blend films, which reveals that the charge carrier transfer and exciton dissociation are enhanced between PDTBT2T-FTBDT and BTP-4F. The Stokes shift can be calculated from the difference between the maximum

absorption and emission, which provides information about a molecule's reorganization energy between the ground and excited-state.^[36] In the printed neat donor films using CF, the Stokes shift values are larger than for the CB printed films (212 nm with CB, 235 nm with CF), indicating that the nonradiative transition of CF printed films consumes more energy than in the CB printed films.^[37] Moreover, the Stokes shift of the donor in the blend film is higher than that of the neat film printed with CB solvent. Probably, the donor exhibits higher nonradiative energy losses when mixed with BTP-4F.

To evaluate the charge transfer process of neat PDTBT2T-FTBDT, BTP-4F as well as the PDTBT2T-FTBDT:BTP-4F blend introduced via using different solvents during the printing, TRPL measurements of the printed films on glass substrates are performed with an excitation wavelength of 405 nm. The TRPL data are shown in Figure 1e,f. They are analyzed with an exponential decay function, where the component of the short lifetime (A_1 , τ_1) corresponds to the fast decay processes, and the long lifetime (A_2 , τ_2) corresponds to the slow decay processes, which are related to trap-assisted recombination and radiative recombination, respectively.^[38] The detailed parameters of TRPL data analysis are summarized Table S1 (Supporting Information). The ratio of A_1/A_2 is calculated to determine the dominant decay process. The value is larger than one for all thin films, which suggests that the fast decay is the main decay process. Notably, in the CF printed films, the ratio is larger than in the CB printed thin films, suggesting that the trap-assisted recombination is enhanced the use of CF as solvent for the printing. The average lifetimes of neat PDTBT2T-FTBDT, BTP-4F, and PDTBT2T-FTBDT:BTP-4F blend are (7.52 ± 0.04) , (5.23 ± 0.03) , and (2.93 ± 0.16) ns if printed out of CB, and (6.29 ± 0.15) , (8.75 ± 0.07) , and (0.85 ± 0.03) ns when processed with CF solvent. For the neat films, the CB printed PDTBT2T-FTBDT film and the CF printed BTP-4F film show a longer lifetime, suggesting reduced recombination in bulk. Interestingly, CF printed PDTBT2T-FTBDT:BTP-4F blend films show a much shorter lifetime, meaning that the radiative recombination is restrained. Thus, a fast charge transport can be induced from PDTBT2T-FTBDT to BTP-4F when printing from CF, which will increase the short circuit current of the corresponding OSCs.

The photovoltaic performance of the OSCs is systematically studied with an inverted device architecture (functional stack is

glass/ITO/ZnO/printed PDTBT2T-FTBDT:BTP-4F/MoO₃/Ag). As shown in Figure 1g and Table 1, solar cells based on the printed active layer using CB solvent shows a relatively low performance with an average efficiency of 6.0 and a V_{oc} of 0.79 V, a J_{sc} of 18.5 mA cm⁻², and an FF of 41.39%. When using CF, the average efficiency increases to 12.8% with a V_{oc} of 0.85 V, a J_{sc} of 23.5 mA cm⁻², and an FF of 64.49%. Notably, the active layer printed with CF solvent exhibits a promising champion PCE of 13.2 % with a J_{sc} of 23.84 mA cm⁻², an FF of 64.49%, and a V_{oc} of 0.85 V at ambient conditions. Thus, all characteristic solar cell parameters J_{sc} , V_{oc} , and FF are improved by the choice of the solvent, which all together contribute to the significantly improved PCE. As seen from the dark J - V curves, the charge carrier recombination of the device is significantly reduced when printed with CF solvent (Figure S1, Supporting Information). To investigate the influence of the atmosphere, solar cells are fabricated under N₂ atmosphere as well, as shown in Table 1; and Figure S2a (Supporting Information). The PCEs of the OSCs are slightly improved for both solvents CB and CF in N₂ atmosphere, which is attributed to the better V_{oc} and FF. Still CF based solar cells are superior in device performance compared to those printed from CB. Moreover, the printed OSCs are also compared with OSCs using an active layer prepared with classical spin-coating in N₂ atmosphere. The highest PCE of 15.4% is achieved in the spin-coated OSCs when using CF solvent, whereas using CB also for spin-coated OSCs results in a lower PCE of 9.9%. Therefore, irrespective of the fabrication method used to deposit the active layer, again CB is a poor solvent for the novel PDTBT2T-FTBDT: BTP-4F blend films based OSCs.

2.2. Film Morphology

The inner structure of the neat PDTBT2T-FTBDT, BTP-4F, and PDTBT2T-FTBDT: BTP-4F blend films printed out of different solvents at ambient conditions is investigated with GISAXS. The 2D GISAXS data are displayed in Figure S3 (Supporting Information). Horizontal line cuts of the 2D GISAXS data are performed at the Yoneda region of PDTBT2T-FTBDT and BTP-4F to investigate characteristic lateral structures. In the neat films, these structures can be understood as crystallite domains in an amorphous polymer or small molecules matrix, giving rise to a scattering contrast. In the blend films, it is characteristic polymer domains in the small molecule matrix. To model the lateral structures, cylindrical and spherical objects with different radii are used in the framework of the distorted wave Born approximation (DWBA) assuming the effective interface approximation (EIA).^[39] The DWBA and EIA-based modeling results are shown in Figure 2b–d. The average large-size domain radii of neat PDTBT2T-FTBDT, BTP-4F, and PDTBT2T-FTBDT: BTP-4F blend films are (100 ± 5) nm, (77 ± 6) nm, and (90 ± 9) nm when using CB, while they are (108 ± 5) nm, (118 ± 5) nm, and (109 ± 4) nm in case of CF. Typically, such large-scale structures are identified as defects in the films.^[30,38] The middle-sized domain radii of neat PDTBT2T-FTBDT, BTP-4F, and PDTBT2T-FTBDT:BTP-4F blend films are (40 ± 3) nm, (23 ± 1) nm, (26 ± 1) nm when using CB, and they are (27 ± 4) nm, (42 ± 1) nm, (23 ± 2) nm in case of CB.

Table 1. Photovoltaic parameters of PDTBT2T-FTBDT:BTP-4F blend devices printed out of CB and CF in ambient and N₂ conditions, respectively. For comparison, the spin-coated devices are shown as well for N₂ conditions. The J - V curves are measured under the illumination of air mass 1.5G at 100 mW cm⁻².

Sample	J_{sc} [mA cm ⁻²]	V_{oc} [V]	FF [%]	PCE _{avg} [%] ^{a)}	PCE _{max} [%]
CB_in ambient	18.5 ± 0.45	0.79 ± 0.02	41.39	6.0 ± 0.6	6.6
CB_in N ₂	16.8 ± 0.42	0.82 ± 0.02	50.25	6.9 ± 0.6	7.4
CB_spin coat	21.8 ± 0.38	0.80 ± 0.02	55.49	9.4 ± 0.5	9.9
CF_in ambient	23.5 ± 0.32	0.85 ± 0.02	64.49	12.8 ± 0.4	13.2
CF_in N ₂	22.3 ± 0.30	0.86 ± 0.02	68.21	13.5 ± 0.4	13.9
CF_spin coat	25.9 ± 0.30	0.84 ± 0.02	69.87	15.1 ± 0.3	15.4

^{a)}Average values are obtained from 10 devices.

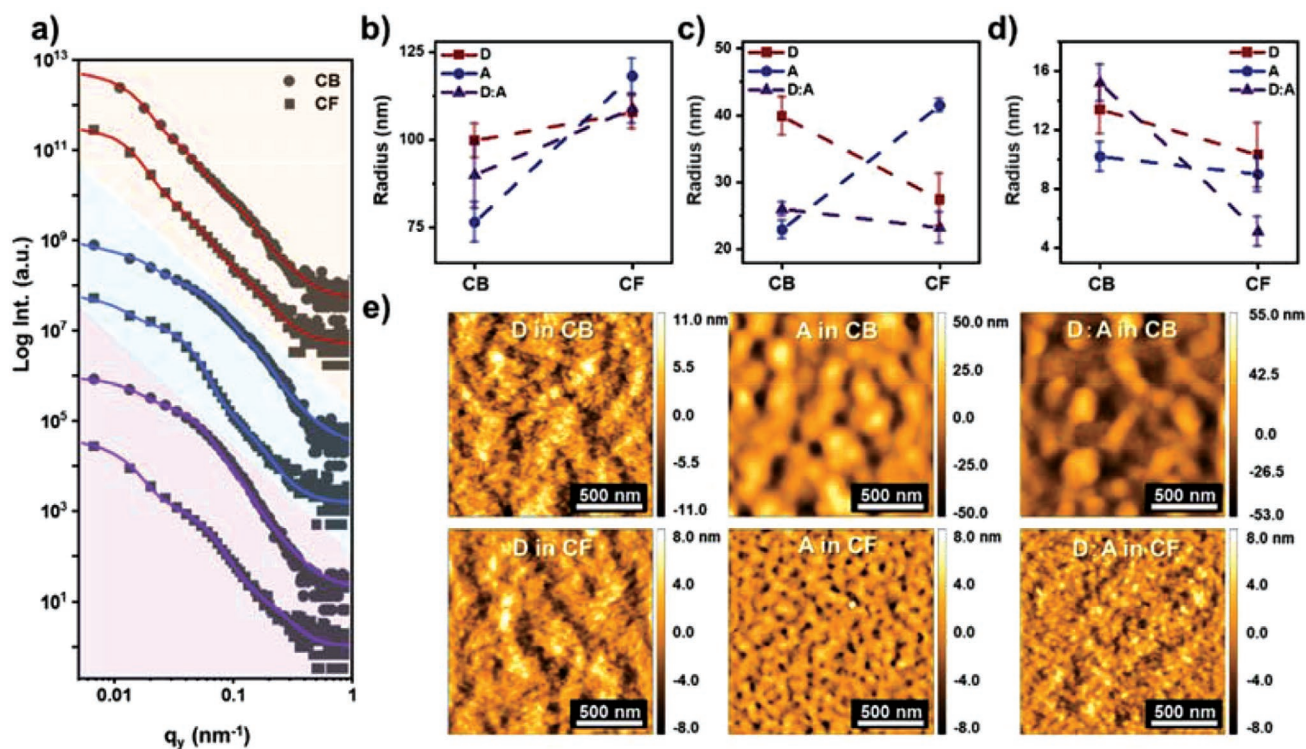


Figure 2. a) Horizontal line cuts of the 2D GISAXS data (symbols) with corresponding fits (solid lines) of the PDTBT2T-FTBDT (red line), BTP-4F (blue line), PDTBT2T-FTBDT:BTP-4F blend (purple line) films printed out of CB (circles) and CF (squares), respectively. Comparison of the average domain radii for the b) large, c) medium, and d) small structures. e) AFM surface topography of printed PDTBT2T-FTBDT, BTP-4F, PDTBT2T-FTBDT: BTP-4F blend films using CB (top row) and CF (bottom row), respectively.

The average small-size domain radii of neat PDTBT2T-FTBDT, BTP-4F, and PDTBT2T-FTBDT: BTP-4F blend films are (13 ± 2) nm, (10 ± 1) nm, (15 ± 1) nm when using CB solvent. They decrease to (10 ± 2) nm, (9 ± 1) nm, (5 ± 1) nm in the case of CF. As shown in Figure 2b, the average large-size domain radius of the PDTBT2T-FTBDT:BTP-4F blend film printed from CB is the smallest among all neat and blend films, suggesting that the blend structure is influenced by both the donor and the acceptor. When using CF instead of CB, the large-size domain radius of the PDTBT2T-FTBDT, BTP-4F, and PDTBT2T-FTBDT:BTP-4F blend film increases. Thus, the large size domains in PDTBT2T-FTBDT:BTP-4F blend films follow the same size as in the neat PDTBT2T-FTBDT films. Consequently, the large structures in the BHJ structure of the blend film are influenced more by the PDTBT2T-FTBDT component than by the BTP-4F component. In contrast, Figure 2c shows that the middle-sized domain radii of the PDTBT2T-FTBDT:BTP-4F blend film decrease when using CF instead of CB, and follow more the trend in the neat PDTBT2T-FTBDT film. For the small-size domain of all the films, the radii decrease in CF. According to previous studies,^[38] domains on the order of tens of nanometers demonstrate a suitable structure size for splitting excitons into charge carriers. Therefore, the blend film printed out of CF shows a better film morphology in terms of characteristic lateral structures as compared with the one printed from CB. Such improved morphology is beneficial for the device performance and explains why the OSCs printed from CF outperform the ones printed from CB.

Besides information about the inner film morphology, the surface topography of the printed films is investigated with AFM (Figure 2e). The root-mean-square (rms) roughness of the neat PDTBT2T-FTBDT film is smaller if printed out of CF (1.9 nm) than out of CB (2.9 nm). The same behavior is found for the neat BTP-4F film. However, the substantial aggregation of BTP-4F in CB results in a very high roughness of 11.9 nm compared with CF (1.6 nm). Accordingly, also the roughness of the PDTBT2T-FTBDT:BTP-4F blend films are 1.6 nm, if printed from CF but 13.2 nm if printed from CB. This significant difference in the surface roughness explains that the surface of the active layer printed out of CF exhibits better contact with the blocking layer and electrode, as well as better miscibility between PDTBT2T-FTBDT and BTP-4F, being beneficial for charge collection in OSCs. Thus, also the smoother film surface contributes to the superior PCE when printed out of CF.

2.3. Crystalline Structure

To measure the crystallite structure in the thin films printed with different solvents at ambient conditions, GIWAXS is performed.^[40] Figure 3a,b shows the 2D GIWAXS data, line profiles and the corresponding Gaussian fits of the neat PDTBT2T-FTBDT, BTP-4F, and PDTBT2T-FTBDT:BTP-4F blend films printed out of CB and CF, respectively. The determined parameters and the calculated stacking distance as well as the crystallite size are listed in Tables S2 and S3 (Supporting Information).

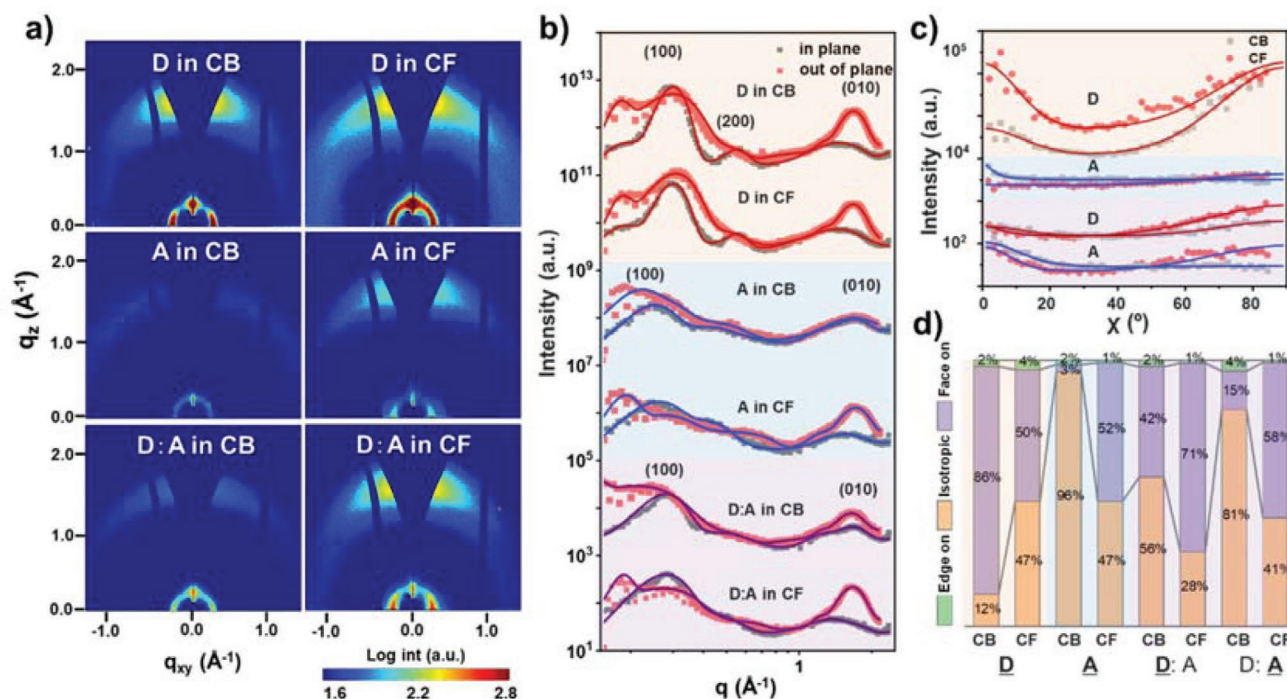


Figure 3. a) 2D GIWAXS data for PDTBT2T-FTBDT, BTP-4F, and PDTBT2T-FTBDT:BTP-4F films printed out of CB and CF. Scattering profiles obtained from b) cake cuts and c) tube cuts in (100) peak of pure PDTBT2T-FTBDT (D), BTP-4F (A) and PDTBT2T-FTBDT:BTP-4F (D:A) films printed out of CB and CF, respectively. Solid lines correspond to the fit of the data. d) Fractions of face-on, edge-on, and isotropically oriented crystallites based on the (100) Bragg peak.

For the wide-bandgap donor polymer PDTBT2T-FTBDT, a (100) Bragg peak is visible at 0.29 \AA^{-1} , corresponding to a d -spacing of 21.7 \AA . The respective (200) Bragg peak at 0.54 \AA^{-1} in the in-plane (IP) direction is also observed for both solvents CB and CF. The (010) Bragg peak in out-of-plane (OOP) direction is seen at 1.69 \AA^{-1} , corresponding to a d -spacing of 3.72 \AA for CB, while it is located at 1.68 \AA^{-1} (d -spacing of 3.74 \AA) for CF. For the BTP-4F film printed out of CB, the (010) Bragg peak is located at 1.71 \AA^{-1} , corresponding to a d -spacing of 3.67 \AA . This Bragg peak is very weak and broadly distributed over the azimuthal angular range, suggesting a low and random distribution of the crystallites with this orientation. In contrast, the BTP-4F film printed out of CF shows a pronounced crystal structure with a face-on orientation. A (100) Bragg peak at 0.25 \AA^{-1} (d -spacing of 25.1 \AA) and a (11-1) Bragg peak at 0.43 \AA^{-1} (d -spacing of 14.6 \AA) in the IP direction as well as a (010) Bragg peak at $\approx 1.72 \text{ \AA}^{-1}$ (d -spacing of 3.65 \AA) in the OOP direction emerge. The different crystallization behavior of the neat thin films manifests to a distinct effect in their blend thin films when printed with different solvents. In case of printing the blend film with CB, the (100) Bragg peak of PDTBT2T-FTBDT is detected at 0.28 \AA^{-1} (d -spacing of 22.4 \AA) and the (100) Bragg peak of BTP-4F is located at 0.20 \AA^{-1} (d -spacing of 31.4 \AA) in the IP direction. The weak (010) Bragg peak of PDTBT2T-FTBDT is at 1.65 \AA^{-1} (d -spacing of 3.81 \AA) and of BTP-4F at 1.71 \AA^{-1} (d -spacing of 3.67 \AA) in the OOP direction. Thus, fewer crystallites are present inside the CB printed film, which is attributed to a hindering of the PDTBT2T-FTBDT crystallization by the crystallization of BTP-4F. On the contrary, the CF printed blend film shows a pronounced (100) Bragg peak of PDTBT2T-FTBDT

at 0.29 \AA^{-1} (d -spacing of 21.7 \AA) in the IP direction together with a (010) Bragg peak at 1.66 \AA^{-1} (d -spacing of 3.79 \AA) in the OOP direction. Moreover, BTP-4F exhibits a (100) Bragg peak at 0.21 \AA^{-1} (d -spacing of 29.9 \AA) concerning the (010) peak of 1.71 \AA^{-1} (d -spacing of 3.67 \AA). Consequently, when printing out of CF, a better face-on structure of crystallites is formed in the active layer than in the case of CB.

To get an insight into the orientation distribution of the crystallite packing, tube cuts are performed from the 2D GIWAXS data (Figure 3c) for the (100) Bragg peaks of PDTBT2T-FTBDT and BTP-4F. The fraction of the face-on, edge-on, and isotropically oriented crystallites is shown in Figure 3d, calculated by integrating the areas of the corresponding features in the pole figures (corrected $I(\chi) \times \sin(\chi)$ vs χ plots in Figures S4–S6 and Tables S4–S5, Supporting Information).^[41,42] For all films, the edge-on orientation occurs only in a minimal fraction. For the face-on orientation, the occurrence depends strongly on the system. Among the thin films printed out of CB, the face-on orientation accounts for 86% of the total crystallites of the neat PDTBT2T-FTBDT thin film, whereas it is only 3% in the neat BTP-4F thin film. In the PDTBT2T-FTBDT:BTP-4F blend film, the face-on orientation in PDTBT2T-FTBDT decreases to 42%, and increases to 15% in BTP-4F. In the thin films printed with CF, the face-on orientation of the neat PDTBT2T-FTBDT is 50% and 52% in the neat BTP-4F thin film. In the blend thin film printed out of CF, the face-on orientation of PDTBT2T-FTBDT increases to 71%, and the face-on orientation of BTP-4F increases to 58%. Thus, the CB printed neat PDTBT2T-FTBDT film exhibits a well-ordered face-on crystal structure with a smaller π - π stacking distance compared to the CF printed neat

PDTBT2T-FTBDT film. However, in the blend film with BTP-4F, the face-on crystallization of PDTBT2T-FTBDT is hindered when using CB. Notably, when the thin films are printed out of CF, the crystal quality in the blend thin film is better than in the neat films, suggesting that the donor and acceptor would facilitate their face-on orientation. Thus, the all over crystallization in the PDTBT2T-FTBDT:BTP-4F blend film is better when printing with CF than with CB as the solvent. The superior crystal structure established when printing out of CF for both, the donor and acceptor, facilitates the charge carrier transport in the blend thin film. Thus high electron mobility and current density can be obtained.^[43]

2.4. Drying Kinetics

To provide a deeper insight into the conformation and aggregation kinetics of the wide-bandgap polymer donor PDTBT2T-FTBDT, the nonfullerene acceptor BTP-4F and the blend of

both (PDTBT2T-FTBDT:BTP-4F), in situ UV-vis measurements are performed during the printing out of CB and CF at ambient conditions, respectively. Since the donor and acceptor have different solubilities in the solvents CF and CB, a different initial aggregation state of the materials can be present in the initial inks. Moreover, due to the different boiling points of the solvent CB (132 °C) and CF (61.2 °C) as well as the big difference in the molecular weights between PDTBT2T-FTBDT and BTP-4F, the molecular assembly of donor and acceptor molecules varies with different solvents as established during the drying process. Compared to CF, films printed from CB undergo a slower film formation, resulting in an increased time for the interaction between donor and donor, acceptor and acceptor, and donor and acceptor (Figure 4a; and Figure S7, Supporting Information). To understand the role of solvent effects on the molecule structure, conformation and aggregation development of the donor and acceptor during the film formation process, the temporal evolution of the PDTBT2T-FTBDT absorption peaks λ_{0-0} and λ_{0-1} as well as of the BTP-4F peaks are determined

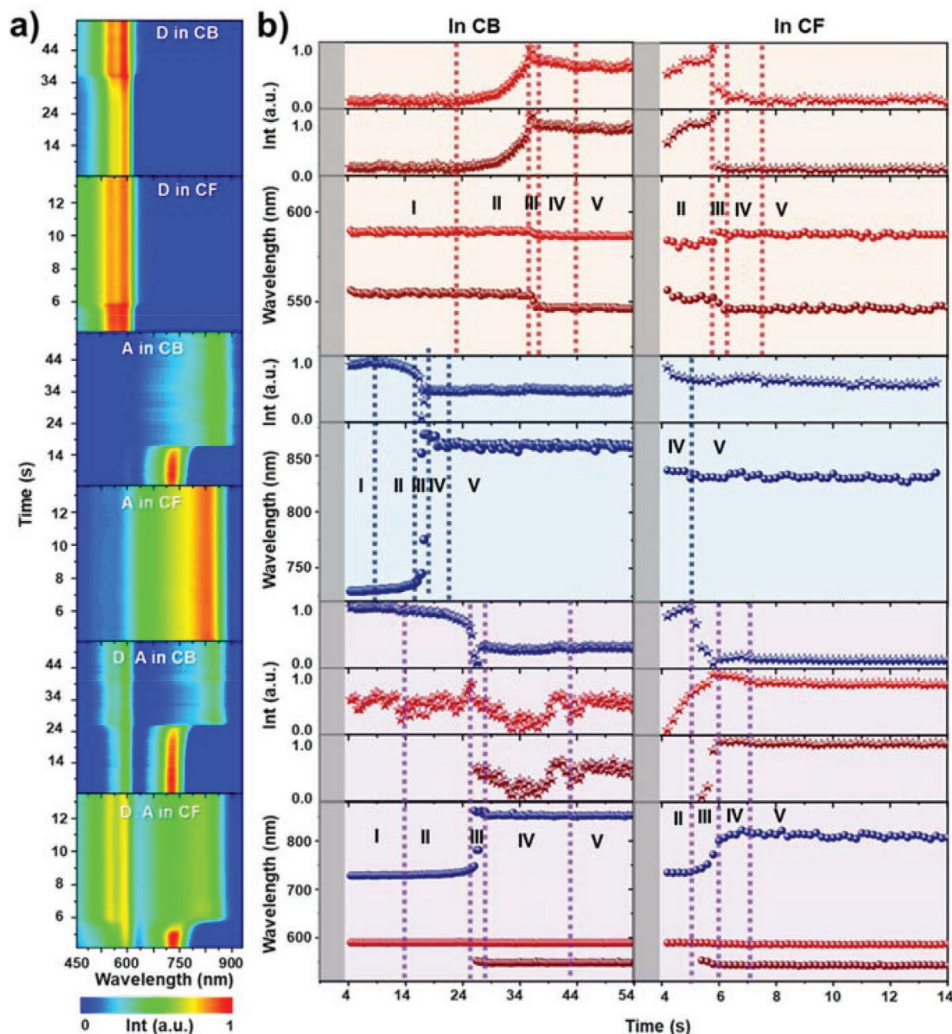


Figure 4. a) In situ UV-vis 2D mapping of the film formation kinetics of neat PDTBT2T-FTBDT, BTP-4F, and PDTBT2T-FTBDT:BTP-4F blend films printed out of CB and CF, respectively. b) Primary peak position (symbols) and the corresponding normalized peak intensity (stars) of neat PDTBT2T-FTBDT (red bulk), neat BTP-4F (blue bulk), and PDTBT2T-FTBDT:BTP-4F (purple bulk) films printed out of CB and CF during the in situ experiment.

(Figure 4b). Due to instrument limitations, we can only observe the film formation kinetics after 4 s.

Similar to the earlier work on another active layer blend film studied in situ during printing, here also five stages are distinguished during the thin film formation.^[24] In stage I, solvent evaporation is dominant with no obvious changes in the peak position and intensity, suggesting that no molecule aggregation occurs during this period.^[44] Notably, stage I is only very prominent for the neat PDTBT2T-FTBDT (≈ 24 s) as well as the PDTBT2T-FTBDT:BTP-4F blend (within ≈ 14 s) films printed out of CB. The initial λ_{0-0} (589 nm) and λ_{0-1} (556 nm) peaks are very distinct in the case of the neat PDTBT2T-FTBDT film, however only the λ_{0-0} peak (592 nm) of PDTBT2T-FTBDT is observed in the blend film. Interestingly, in case of the neat BTP-4F film, the spectrum (maximum at 729 nm) shows a red shift and concomitantly gains intensity. This tiny spectral change and the increase in intensity signify a planarization of the disordered chains that leads to an increased conjugation length. For CF, stage I is not resolved. In stage II, upon further solvent evaporation, average solute structures start to interact with each other. The PDTBT2T-FTBDT (in CB and CF) and BTP-4F (blend in CF) peaks are growing in intensity and exhibit a sharp absorption spectrum, which is attributed to an ordered chain conformation. For BTP-4F in CB a red shift is seen from 732 to 743 nm in the neat thin film after 7 s and from 729 to 745 nm in the blend thin film after 14 s. This red shift is accompanied by a decrease in the intensity, suggesting a disordered chain conformation.^[45] In stage III, the majority of the solvent has evaporated and the absorption peak positions begin to shift concerning their initial values due to a rapid aggregate formation. Thus, this stage can be attributed to an order-disorder phase transition.^[28] The λ_{0-1} peak of PDTBT2T-FTBDT in the neat film blue shifts to 546 nm after 20 s printing out of CB and to 545 nm after 5 s printing with CF. In contrast, the λ_{0-0} peak of PDTBT2T-FTBDT slightly blue shifts to 586 nm in case of CB and red shifts to 589 nm in case of CF, suggesting that the CB solvent is more favorable for an H-aggregate formation of the neat PDTBT2T-FTBDT polymer. Contrary to PDTBT2T-FTBDT, the absorption peak of BTP-4F (shift from 743 to 869 nm after 20 s) exhibits a J-aggregated transition behavior in CB. The arising of a new peak at a higher wavelength (852 nm) is associated with a further planarization of the aggregated chain segments during solvent evaporation. In the blend thin film printed out of CB, the PDTBT2T-FTBDT λ_{0-0} peak intensity slightly decreases together with a peak blue shift to 589 nm. The λ_{0-1} peak evolves and blue shifts from 554 to 549 nm with a simultaneous intensity decrease. The absorption peak of BTP-4F slightly red shifts till 745 nm with a decreasing intensity to a minimum value. Meanwhile, a new peak attributed to BTP-4F arises at 852 nm and then shifts toward 857 nm with increasing intensity. In the case of the blend printed from CF, the PDTBT2T-FTBDT λ_{0-0} peak slightly blue shifts from 589 to 587 nm with an intensity increase reaching a maximum value. The λ_{0-1} peak of PDTBT2T-FTBDT appears then shifting from 553 to 544 nm with an intensity increase reaching a maximum. The absorption peak of BTP-4F rises to its highest intensity. Then it shifts strongly from 734 to 800 nm, with a decreasing intensity to its minimum. All these strong changes in the absorption spectrum demonstrate that stage III is very

crucial for the quality of the printed thin films. In total, the neat PDTBT2T-FTBDT exhibits a well-ordered conformation in CB, and the neat BTP-4F exhibits a better aggregation in CF, respectively. Notably, the PDTBT2T-FTBDT:BTP-4F blends manifest a better-ordered conformation than the corresponding neat thin films in CF (less pronounced in CB solvent), which could be a synergistic effect. In stage IV, the absorption peaks of the PDTBT2T-FTBDT remain constant in their positions but change in their intensity. The spectrum boarding suggests a planarization of the aggregated phase. The BTP-4F peaks slightly blue shift with an intensity decrease in CB solvent and the neat BTP-4F in CF, suggesting a favorable planarization of the H-aggregated phase.^[45,46] Then, the BTP-4F peak further red shifts to 822 nm accompanied by the intensity slightly increasing in the blend thin film printed out of CF, indicating an enhancement of the ordered structure for the J-aggregates. Interestingly, we observe a decrease followed by an increase in the signal from the donor in CB for the blend thin film, suggesting that the presence of BTP-4F has a stabilizing influence on the conformation of PDTBT2T-FTBDT. In stage V, almost all solvent is fully evaporated and no more changes in the peak positions and peak intensities suggest no further transition or aggregation among all materials.

To study the real-time evolution of the crystal structure of the PDTBT2T-FTBDT:BTP-4F blend films printed with both solvents at ambient conditions, in situ GIWAXS measurements are carried out. Selected 2D GIWAXS data of the film formation are shown in Figures S8 and S9 (Supporting Information). Line profiles with the corresponding Gaussian fits of the (010) Bragg peaks in the OOP direction from the 2D GIWAXS data are shown in Figure 5a,d. In Figure 5a, the intense and broad ring located around 1.3 \AA^{-1} originates mainly from the scattering of the CB solvent, which is in agreement with earlier studies.^[47] As the solvent evaporates, the scattering contribution of CB is reduced, whereas the (010) Bragg peak of the crystallites in the blend located at $\approx 1.6\text{--}1.8 \text{ \AA}^{-1}$ becomes more and more distinct. As seen in Figure 5d, the (010) Bragg peak becomes more pronounced with increased intensity and a slight shift from its initial position. These changes suggest the formation of a face-on crystallite orientation undergoing slight compaction during the CF evaporation. To give insights into the crystallite formation of the donor and acceptor in different solvents, the development in the (010) Bragg peak extracted from the Gaussian fits provides information about the intensity, the $\pi\text{--}\pi$ stacking distance (calculated by $2\pi q^{-1}$) as well as the crystallite size (estimated by the Debye-Scherrer equation) as shown in Figure 5b,c (CB solvent) as well as Figure 5e,f (CF solvent).^[41] The formation of the (010) OOP crystallites also exhibits five different stages in agreement with the in situ UV-vis data, although the first stage is not resolved in the case of CF. This first stage is the solvent evaporation stage. During stage I, no obvious crystal growth is observed for CB due to the presence of excess host solvent and absence of crystallization.^[28] However, a certain amount of initial crystals is existing in stage I with donor crystallite sizes of about 2.4 nm and a $\pi\text{--}\pi$ stacking distance of 3.7 Å, as well as a size of the acceptor crystals of about 1.6 nm and a stacking distance of 3.4 Å. Thus, a preaggregation of donor and acceptor happened in CB as well as in CF. At stage II, the crystallite size increases progressively in both solvents, suggesting moderate

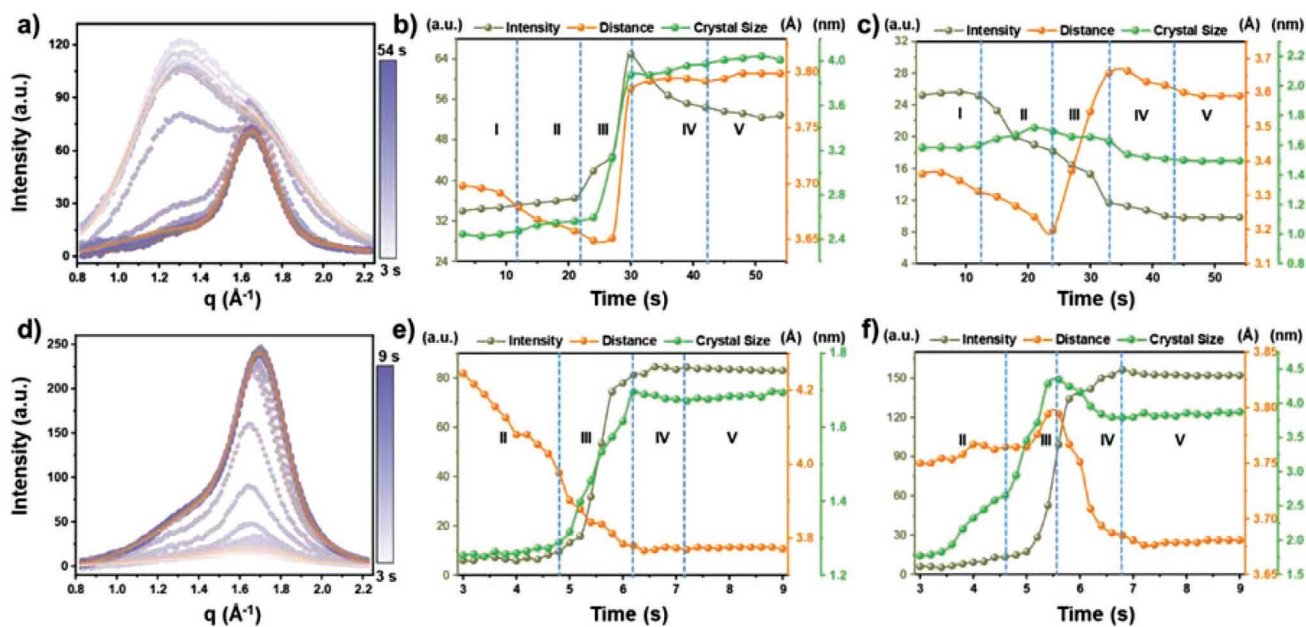


Figure 5. a) Sector integrals (0° – 15°) and the corresponding fits of the in situ 2D GIWAXS data of the PDTBT2T-FTBDT:BTP-4F blend film printed out of CB. Evolution of the out-of-plane (010) Bragg peak of b) PDTBT2T-FTBDT and c) BTP-4F in the blend film printed out of CB. d) Sector integrals (0° – 15°) and the corresponding fits of the in situ 2D GIWAXS data of the PDTBT2T-FTBDT:BTP-4F blend film printed out of CF. Evolution of the out-of-plane (010) Bragg peak of e) PDTBT2T-FTBDT and f) BTP-4F in case of CF.

crystal growth. In addition, the (010) π – π stacking distance of the donor and acceptor decreases with the ongoing evaporation of the solvent, causing more close packing of the crystals. Only for BTP-4F in CF an increase in the stacking distance is seen in stage II. The intensity of the Bragg peak related to BTP-4F decreases in CB while it increases in CF, showing that in CB the small molecule crystallization is hindered. For PDTBT2T-FTBDT, the intensity increases only moderately, meaning that the donor polymer is only slowly crystallizing in this stage. In contrast, in stage III where the phase transition happens, for the donor in CB, the Bragg peak intensity, the crystallite size as well as the π – π stacking distance increase massively, indicating a rapid but imperfect crystal growth of the donor. For the acceptor in CB, the intensity and the crystallite size slightly decrease while the stacking distance increases, suggesting a perturbation of the BTP-4F crystallites caused by the PDTBT2T-FTBDT crystallization. For the donor in CF, the Bragg peak intensity and the crystallite size also increase significantly while the π – π stacking distance is further decreasing. Thus, the amount of donor crystallites grows rapidly in conjunction with crystal growth and an improvement of the inner order. For the acceptor in CF, the intensity and the size as well as the stacking distance increase. Thus, the small molecule crystallization is hindered by the polymer crystallization. In stage IV, for CB the intensity of the Bragg peak of the donor decreases while crystallite size and stacking distance slightly increase, suggesting the stabilization of the crystallites.^[47] For the acceptor, the intensity increases slightly, crystallite size decreases, and the stacking distance remains unchanged. In contrast, in case of CF the intensity, crystallite size, and stacking distance of the donor all slightly decrease, whereas for the acceptor, the intensity increases but size and distance decrease. Finally, all the

solvent molecules left the film, the film turns glassy and the film formation stops (stage V) as seen by the constant intensity, distance, and size.

To determine the temporal orientation evolution of the donor and acceptor crystallites in the films printed with different solvents, we perform the (100) peak tube cuts from the in situ 2D GIWAXS data measured during the printing. **Figure 6a–d** shows the corresponding tube cuts data. The change of the face-on, edge-on, as well as isotropic orientation are determined during the film formation (Figure 6e–h). Since the edge-on orientation is not prominent in the films irrespective of the used solvent, it is not further discussed here. During stage I, no obvious changes in crystallite orientation are observed, in agreement with a solvent-rich film. In good agreement with the in situ UV–vis data, the contribution of isotropic crystallites already exists in stage I for CB. In stage II, PDTBT2T-FTBDT, as well as BTP-4F start to aggregate in both solvents, exhibiting a slight increase in the isotropic orientation. In addition, the face-on crystallite orientation appears and grows with time, while it is still less than the isotropic phase. In stage III, the isotropic and the face-on phase grow strongly in all samples due to the rapid crystal growth (around 23–30 s in CB and 5–6 s in CF). For CB, the isotropic PDTBT2T-FTBDT crystallites increase by about 4 times more and the face-on oriented PDTBT2T-FTBDT crystallites by roughly 8 times, with still the isotropic orientation being the majority.

Similarly, also the isotropic orientation of BTP-4F dominates (increases about 6 times, whereas the face-on orientation grows by a factor of two). In contrast, in CF, the isotropic orientation is less dominant and surpassed by the face-on oriented crystallites. In stage IV, the isotropic phase decreases slightly in PDTBT2T-FTBDT and BTP-4F for CB and CF, respectively. In

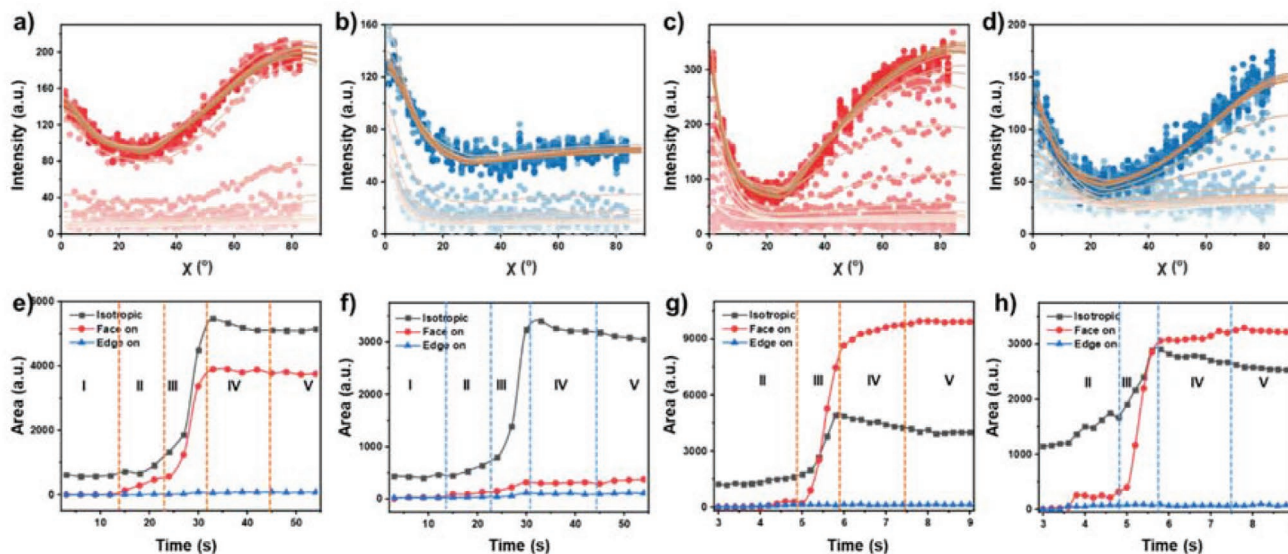


Figure 6. Azimuthal tube cuts of the in situ 2D GIWAXS data taken at the (100) peak of a) PDTBT2T-FTBDT and of b) BTP-4F for the blend films printed out of CB, as well as c) PDTBT2T-FTBDT and d) BTP-4F printed out of CF. Evolution of the (100) crystallite orientation area of e) the donor PDTBT2T-FTBDT and the acceptor f) BTP-4F using CB, as well as the g) PDTBT2T-FTBDT and h) BTP-4F using CF, respectively.

addition, the face-on phase is almost constant in CB, while it further increases in CF. Again, stage V means no more change in the distribution of the crystallite orientations.

3. Conclusion

Based on the study of the respective neat donor and acceptor films, systematic research of the effect of the donor–acceptor interplay on the absorbance, exciton dissociation, charge transfer, exciton kinetics, nanoscale morphology, and crystallinity of printed PDTBT2T-FTBDT:BTP-4F active layers is performed to provide insights into the related device performance of wide-bandgap nonfullerene acceptor based OSCs. The best performing devices are achieved with printing out of CF due to the best-suited nanoscale morphology, the presence of well-ordered crystallites, a lower surface roughness and a higher exciton dissociation probability. The relatively poor performance of slot-die coated devices printed from CB is attributed to the imbalanced crystallinity of the PDTBT2T-FTBDT and BTP-4F phases in the BHJ structure inhibiting an efficient exciton diffusion and free charge carrier transport. Moreover, in situ UV–vis and in situ GIWAXS measurements give insights into the film formation kinetics related to the structure conformation, aggregation, and crystallite structure, as well as crystallite orientation. We find that the conformational evolution of donor and acceptor is different. PDTBT2T-FTBDT preferentially forms H-aggregates and in contrast, BTP-4F prefers J-aggregates formation during solvent evaporation.

Interestingly, the aggregate formation of PDTBT2T-FTBDT and BTP-4F causes a synergistic effect when printing out of CF. Therefore, the donor and acceptor in the blend thin films manifest a pronounced, well-ordered crystallite growth with a majority of the crystallites being face-on orientated. In contrast, the synergistic effect in the donor and acceptor crystallization is

absent when printing out of CB, mainly because BTP-4F experiences an excessive J-aggregation. The unbalanced crystallization of donor and acceptor gives rise to a more disordered orientation with a reduced donor crystal quality. In the late stage of the film formation, isotropic donor and acceptor crystallites order in face-on orientation for CF, whereas for CB this improvement in the film is absent. Thereby, with printing in ambient conditions, OSCs with PCE of 13.2% are demonstrated when using CF without the need for energy consuming postproduction steps like annealing. Thus, this work reveals valuable insights into the solvent effects on the donor–acceptor morphology and the mechanism of film formation kinetics in the field of nonfullerene OSCs, which cause significant differences in the related device performance. Since the OSCs are printed via the slot-die coating technique in ambient atmosphere, the findings offer great practical perspectives for bringing OSCs into real-world applications.

4. Experimental Section

Materials: The wide-bandgap donor polymer poly[2,2'-(bis[[[2-butyl(octyl)oxy]carbonyl][2,2':5',2'':5'',2'''-quaterthiophene]-5,5''-diyl] (PDTBT2T-FTBDT or sometimes called D18) and the nonfullerene acceptor 2,2'-(2Z,2'Z)-((12,13-bis(2-ethylhexyl)-3,9-diundecyl-12,13-dihydro [1,2,5]thiadiazolo[3,4-e]thieno[2'',3'':4',5']thieno[2',3':4,5]pyrrolo[3,2-g]thieno[2',3':4,5]thieno[3,2-b]indole-2,10-diyl)bis(methanylylidene))bis(5,6-difluoro-3-oxo-2,3-dihydro-1H-indene-2,1-diylidene))dimalononitrile (BTP-4F or sometimes called Y6) were purchased from 1-Material Inc.. For simplicity, the PDTBT2T-FTBDT is labeled as D, the BTP-4F is labeled as A in the figures and tables. Chloroform (CF, >99.8%) and chlorobenzene (CB, >99.8%) were obtained from Sigma-Aldrich Inc. Laser pattern ITO substrates with a sheet resistance of 15 Ω cm⁻² were purchased from Advanced Election Technology CO, Ltd. All reagents and solids were used as received without any further purification.

Sample Preparation: PDTBT2T-FTBDT:BTP-4F blend films based on different solvents were fabricated as follows: PDTBT2T-FTBDT and

BTP-4F were dissolved in CF or CB with a total concentration of 8 mg mL⁻¹ (11 mg mL⁻¹ for the spin-coated samples) and stirred at 38 °C for at least 4 h. Then the donor and the acceptor were mixed with a ratio of 1:1.6 in weight and the mixture was kept stirring for at least 4 h under 38 °C. Subsequently, these solutions were printed at ambient conditions on cleaned silicon substrates with a print speed of 5 mm s⁻¹ and a flow rate of 0.1 mL min⁻¹ using a custom-made slot-die coater.^[48] A print head distance of 150 μm was installed to realize films with a thickness between 80 and 90 nm. Neat PDTBT2T-FTBDT and BTP-F4 films were prepared under identical conditions by using the initial CF or CB solutions.

Devices Fabrication: Solar cells based on PDTBT2T-FTBDT:BTP-4F were fabricated with an inverted device architecture as glass/ITO/ZnO/PDTBT2T-FTBDT:BTP-4F/MoO₃/Ag, as shown in Figure S11 (Supporting Information). 30 nm ZnO layer was spin-coated on a clean ITO substrate with a post-annealing treatment for 40 min in air as previous work.^[38] Then the solution of the active layer was printed on the top of the ZnO layer by a slot-die coater at ambient conditions. The film thickness of the active layer was controlled at around 80–90 nm by adjusting the print parameters. The active layer was dried in ambient conditions without any post-treatment process (thermal annealing, solvent vapor annealing, etc.). Afterward, the samples were transferred into a nitrogen-filled glove box and 8 nm of MoO₃ and 100 nm of Ag electrode were deposited on the active layer in sequence by thermal evaporation. For the N₂ atmosphere printed devices, the active layers were fabricated with the slot-die coater and dried inside a N₂ filled chamber with a N₂ flow rate of 30 sccm during printing. For the spin-coated devices, the active layer was spin-coated and dried inside a N₂ glovebox, with the thickness being around 90 nm.

Characterizations: Static UV–vis measurements were conducted with a Lambda 650 S UV–vis spectrometer (PerkinElmer) in transmission mode at ambient conditions. Photoluminescence (PL) spectroscopy measurements were carried out on a custom-built setup, comprising of a 405 nm diode laser (iBeam, Toptica Photonics) for excitation and a liquid nitrogen cooled CCD (Symphony II, Horiba) mounted to a spectrometer (iHR550, Horiba) for detection. The excitation as well as detection light was routed through the same microscopy objective (UMPlanFL 50x, NA: 0.8, Olympus) in a geometry similar to fluorescence microscopy. Time-resolved photoluminescence spectroscopy (TRPL) was performed using a time-correlated single photon counting (TCSPC) system integrated in the aforementioned photoluminescence setup. The samples were excited with a 405 nm pulsed diode laser (LDH-P-C-405B, PicoQuant) at a repetition rate of 10 MHz. The signal was detected using an avalanche photodiode (PDM PD-100-CTE, Micro Photon Devices) mounted to the secondary exit of the spectrometer. The decay lifetimes were analyzed by reconvolution using the software EasyTau 2 (Picoquant). The instrument response function necessary for this fit procedure was recorded at a wavelength of 700 nm using a dilute solution of Allura Red AC.^[49] The *J*–*V* measurements of the OSCs were carried out under AM1.5 irradiation using a solar simulator (LOT-QuantumDesign GmbH.) with a power density of 100 mW cm⁻² at ambient conditions. The effective illumination area of the device was 0.152 cm² fixed by an opaque mask. The atomic force microscope (AFM) images were collected by using an AFM instrument (MFP-3D, Asylum Research) in tapping mode using conical-shaped tips with a radius of 7 nm. For the GISAXS/GIWAXS measurements, the Ganesha SAXSLAB instrument was used with the X-ray energy of 8.047 keV (1.54 Å) at TU Munich. The SDD was set to 1045 mm with an incident angle of 0.35° for the collection of the GISAXS data. For static GIWAXS, the SDD was 95 mm with an incident angle of 0.2°. In situ UV–vis spectroscopy was performed using a CAS 140 CT Instrument Systems Compact Array spectrometer and an MBB1D1 broadband light-emitting diode (THORLABS), which was installed below the sample holder inside the slot-die coater. The in situ GIWAXS measurements were carried out at the P03 beamline, PETRA III, DESY in Hamburg (Germany), using an X-ray beam wavelength of 0.99 Å (energy of 12.57 keV).^[50] For the in situ GIWAXS measurements, the SDD was 180 mm and the incident angle was 0.11°.

Supporting Information

Supporting Information is available from the Wiley Online Library or from the author.

Acknowledgements

This work was supported by funding from the Deutsche Forschungsgemeinschaft (DFG, German Research Foundation) Grant No. Mu1487/22, the International Research Training Group 2022 Alberta/Technical University of Munich International Graduate School for Environmentally Responsible Functional Hybrid Materials (ATUMS) and under Germany's Excellence Strategy – EXC 2089/1 – 390776260 (e conversion), TUM.solar in the context of the Bavarian Collaborative Research Project Solar Technologies Go Hybrid (SolTech) and the Center for NanoScience (CeNS). X.J., S.T., and S.Y. acknowledge the China Scholarship Council (CSC) and P.C. the Erasmus Mundus MaMaSELF+ program for financial support. Parts of this research were carried out at the light source PETRA III at DESY, a member of the Helmholtz Association (HGF). The authors thank Prof. Alexander Holleitner and Peter Weiser for offering the opportunity to perform AFM measurements.

Open access funding enabled and organized by Projekt DEAL.

Conflict of Interest

The authors declare no conflict of interest.

Data Availability Statement

The data that support the findings of this study are available from the corresponding author upon reasonable request.

Keywords

charge carrier kinetics, in situ GIWAXS, in situ UV–vis, nonfullerene OSCs, slot-die coating

Received: December 20, 2021

Revised: February 7, 2022

Published online: February 27, 2022

- [1] J. Hou, O. Inganäs, R. H. Friend, F. Gao, *Nat. Mater.* **2018**, *17*, 119.
- [2] K. Weng, L. Ye, L. Zhu, J. Xu, J. Zhou, X. Feng, G. Lu, S. Tan, F. Liu, Y. Sun, *Nat. Commun.* **2020**, *11*, 2855.
- [3] T. Wang, R. Sun, M. Shi, F. Pan, Z. Hu, F. Huang, Y. Li, J. Min, *Adv. Energy Mater.* **2020**, *10*, 2000590.
- [4] Z. Zhang, Y. Li, G. Cai, Y. Zhang, X. Lu, Y. Lin, *J. Am. Chem. Soc.* **2020**, *142*, 18741.
- [5] Y. Huang, N. Zheng, Z. Wang, L. Ying, F. Huang, Y. Cao, *Chem. Commun.* **2017**, *53*, 1997.
- [6] Y. Lin, J. Wang, Z.-G. Zhang, H. Bai, Y. Li, D. Zhu, X. Zhan, *Adv. Mater.* **2015**, *27*, 1170.
- [7] S. Zhang, Y. Qin, J. Zhu, J. Hou, *Adv. Mater.* **2018**, *30*, 1800868.
- [8] W. Zhao, S. Li, H. Yao, S. Zhang, Y. Zhang, B. Yang, J. Hou, *J. Am. Chem. Soc.* **2017**, *139*, 7148.
- [9] Y. Zhang, Y. Cho, J. Lee, J. Oh, S.-H. Kang, S. M. Lee, B. Lee, L. Zhong, B. Huang, S. Lee, J.-W. Lee, B. J. Kim, Y. Li, C. Yang, *J. Mater. Chem. A* **2020**, *8*, 13049.
- [10] L. Gao, Z.-G. Zhang, H. Bin, L. Xue, Y. Yang, C. Wang, F. Liu, T. P. Russell, Y. Li, *Adv. Mater.* **2016**, *28*, 8288.

- [11] M. Zhang, X. Guo, W. Ma, H. Ade, J. Hou, *Adv. Mater.* **2015**, *27*, 4655.
- [12] J. Yuan, Y. Zhang, L. Zhou, G. Zhang, H. L. Yip, T. K. Lau, X. Lu, C. Zhu, H. Peng, P. A. Johnson, M. Leclerc, Y. Cao, J. Ulanski, Y. Li, Y. Zou, *Joule* **2019**, *3*, 1140.
- [13] Q. Liu, Y. Jiang, K. Jin, J. Qin, J. Xu, W. Li, J. Xiong, J. Liu, Z. Xiao, K. Sun, S. Yang, X. Zhang, L. Ding, *Sci. Bull.* **2020**, *65*, 272.
- [14] S. Dong, T. Jia, K. Zhang, J. Jing, F. Huang, *Joule* **2020**, *4*, 2004.
- [15] H. Kang, G. Kim, J. Kim, S. Kwon, H. Kim, K. Lee, *Adv. Mater.* **2016**, *28*, 7821.
- [16] C. J. Schaffer, C. M. Palumbiny, M. A. Niedermeier, C. Burger, G. Santoro, S. V. Roth, P. Müller-Buschbaum, *Adv. Energy Mater.* **2016**, *6*, 1600712.
- [17] L. Hong, H. Yao, Z. Wu, Y. Cui, T. Zhang, Y. Xu, R. Yu, Q. Liao, B. Gao, K. Xian, H. Y. Woo, Z. Ge, J. Hou, *Adv. Mater.* **2019**, *31*, 1903441.
- [18] W. Zhao, S. Zhang, Y. Zhang, S. Li, X. Liu, C. He, Z. Zheng, J. Hou, *Adv. Mater.* **2018**, *30*, 1704837.
- [19] Y. Galagan, J.-E. J. M. Rubingh, R. Andriessen, C.-C. Fan, P. W. M. Blom, S. C. Veenstra, J. M. Kroon, *Sol. Energy Mater. Sol. Cells* **2011**, *95*, 1339.
- [20] S. Song, K. T. Lee, C. W. Koh, H. Shin, M. Gao, H. Y. Woo, D. Vak, J. Y. Kim, *Energy Environ. Sci.* **2018**, *11*, 3248.
- [21] W. Zhao, Y. Zhang, S. Zhang, S. Li, C. He, J. Hou, *J. Mater. Chem. C* **2019**, *7*, 3206.
- [22] J. Lee, Y.-H. Seo, S.-N. Kwon, D.-H. Kim, S. Jang, H. Jung, Y. Lee, H. Weerasinghe, T. Kim, J. Y. Kim, D. Vak, S.-I. Na, *Adv. Energy Mater.* **2019**, *9*, 1901805.
- [23] S. Dong, K. Zhang, T. Jia, W. Zhong, X. Wang, F. Huang, Y. Cao, *Eco Mat.* **2019**, *1*, 12006.
- [24] K. S. Wienhold, C. L. Weindl, S. Yin, T. Tian, M. Schwartzkopf, A. Rothkirch, S. V. Roth, P. Müller-Buschbaum, *ACS Appl. Mater. Interfaces* **2020**, *12*, 40381.
- [25] S. Rasool, D. van Vu, C. E. Song, H. K. Lee, S. K. Lee, J.-C. Lee, S.-J. Moon, W. S. Shin, *Adv. Energy Mater.* **2019**, *9*, 1900168.
- [26] H. W. Ro, J. M. Downing, S. Engmann, A. A. Herzing, D. M. DeLongchamp, L. J. Richter, S. Mukherjee, H. Ade, M. Abdelsamie, L. K. Jagadamma, A. Amassian, Y. Liu, H. Yan, *Energy Environ. Sci.* **2016**, *9*, 2835.
- [27] D. Vak, K. Hwang, A. Faulks, Y.-S. Jung, N. Clark, D.-Y. Kim, G. J. Wilson, S. E. Watkins, *Adv. Energy Mater.* **2015**, *5*, 1401539.
- [28] H. Zhao, H. B. Naveed, B. Lin, X. Zhou, J. Yuan, K. Zhou, H. Wu, R. Guo, M. A. Scheel, A. Chumakov, S. V. Roth, Z. Tang, P. Müller-Buschbaum, W. Ma, *Adv. Mater.* **2020**, *32*, 2002302.
- [29] D. Zheng, X.-A. Yuan, H. Ma, X. Li, X. Wang, Z. Liu, J. Ma, R. Soc. *Open Sci.* **2018**, *5*, 171928.
- [30] K. S. Wienhold, V. Körstgens, S. Grott, X. Jiang, M. Schwartzkopf, S. V. Roth, P. Müller-Buschbaum, *ACS Appl. Mater. Interfaces* **2019**, *11*, 42313.
- [31] Z. Cao, S. Yang, B. Wang, X. Shen, G. Han, Y. Yi, *J. Mater. Chem. A* **2020**, *8*, 20408.
- [32] Z. Wang, Z. Peng, Z. Xiao, D. Seyitliyev, K. Gundogdu, L. Ding, H. Ade, *Adv. Mater.* **2020**, *32*, 2005386.
- [33] A. A. Meresa, F. S. Kim, *Polymers* **2020**, *12*, 128.
- [34] J. Huang, Z. Chen, Z. Mao, D. Gao, C. Wei, Z. Lin, H. Li, L. Wang, W. Zhang, G. Yu, *Adv. Electron. Mater.* **2017**, *3*, 1700078.
- [35] N. J. Hestand, F. C. Spano, *Chem. Rev.* **2018**, *118*, 7069.
- [36] Z.-P. Yu, Z.-X. Liu, F.-X. Chen, R. Qin, T.-K. Lau, J.-L. Yin, X. Kong, X. Lu, M. Shi, C.-Z. Li, H. Chen, *Nat. Commun.* **2019**, *10*, 2152.
- [37] M. Li, A. H. Balawi, P. J. Leenaers, L. Ning, G. H. L. Heintges, T. Marszalek, W. Pisula, M. M. Wienk, S. C. J. Meskers, Y. Yi, F. Laquai, R. A. J. Janssen, *Nat. Commun.* **2019**, *10*, 2867.
- [38] X. Jiang, H. Kim, P. S. Deimel, W. Chen, W. Cao, D. Yang, S. Yin, R. Schaffrinna, F. Allegretti, J. V. Barth, M. Schwager, H. Tang, K. Wang, M. Schwartzkopf, S. V. Roth, P. Müller-Buschbaum, *J. Mater. Chem. A* **2020**, *8*, 23628.
- [39] D. Yang, F. C. Löhner, V. Körstgens, A. Schreiber, B. Cao, S. Bernstorff, P. Müller-Buschbaum, *Adv. Sci.* **2020**, *7*, 2001117.
- [40] D. Yang, B. Cao, V. Körstgens, N. Saxena, N. Li, C. Bilko, S. Grott, W. Chen, X. Jiang, J. E. Heger, S. Bernstorff, P. Müller-Buschbaum, *ACS Appl. Energy Mater.* **2020**, *3*, 2604.
- [41] K. A. Page, A. Kusoglu, C. M. Stafford, S. Kim, R. J. Kline, A. Z. Weber, *Nano Lett.* **2014**, *14*, 2299.
- [42] J. L. Baker, L. H. Jimison, S. Mannsfeld, S. Volkman, S. Yin, V. Subramanian, A. Salleo, A. P. Alivisatos, M. F. Toney, *Langmuir* **2010**, *26*, 9146.
- [43] L. Zhu, M. Zhang, G. Zhou, T. Hao, J. Xu, J. Wang, C. Qiu, N. Prine, J. Ali, W. Feng, X. Gu, Z. Ma, Z. Tang, H. Zhu, L. Ying, Y. Zhang, F. Liu, *Adv. Energy Mater.* **2020**, *10*, 1904234.
- [44] B. Lin, X. Zhou, H. Zhao, J. Yuan, K. Zhou, K. Chen, H. Wu, R. Guo, M. A. Scheel, A. Chumakov, S. V. Roth, Y. Mao, L. Wang, Z. Tang, P. Müller-Buschbaum, W. Ma, *Energy Environ. Sci.* **2020**, *13*, 2467.
- [45] F. Panzer, H. Bässler, A. Köhler, *J. Phys. Chem. Lett.* **2017**, *8*, 114.
- [46] M. Li, C. An, T. Marszalek, M. Baumgarten, H. Yan, K. Müllen, W. Pisula, *Adv. Mater.* **2016**, *28*, 9430.
- [47] D. Yang, S. Grott, X. Jiang, K. S. Wienhold, M. Schwartzkopf, S. V. Roth, P. Müller-Buschbaum, *Small Methods* **2020**, *4*, 2000418.
- [48] K. S. Wienhold, V. Körstgens, S. Grott, X. Jiang, M. Schwartzkopf, S. V. Roth, P. Müller-Buschbaum, *Sol. RRL* **2020**, *4*, 2000086.
- [49] R. Chib, S. Shah, Z. Gryczynski, R. Fudala, J. Borejdo, B. Zelent, M. G. Corradini, R. D. Ludescher, I. Gryczynski, *Meas. Sci. Technol.* **2016**, *27*, 27001.
- [50] A. Buffet, A. Rothkirch, R. Döhrmann, V. Körstgens, M. M. Abul Kashem, J. Perlich, G. Herzog, M. Schwartzkopf, R. Gehrke, P. Müller-Buschbaum, S. V. Roth, *J. Synchrotron Radiat.* **2012**, *19*, 647.